COMMUNICATION

Check for updates

Carbonic anhydrase IX-targeted nanovesicles potentiated ferroptosis by remodeling the intracellular environment for synergetic cancer therapy†

Nian Liu,[a] Qian Lin,[a] Wenbao Zuo,[a] Weibin Chen,[b] Shan Huang,[c] Yinshu Han,[c] Xing-Jie Liang, [ID] *[ade] Xuan Zhu*[a] and Shuaidong Huo [ID] *[a]

Ferroptosis is one critical kind of regulated cell death for tumor suppression, yet it still presents challenges of low efficiency due to the intracellular alkaline pH and aberrant redox status. Herein, we reported a carbonic anhydrase IX (CA IX)-targeted nanovesicle (PAHC NV) to potentiate ferroptosis by remodeling the intracellular environment. CA IX inhibitor 4-(2-aminoethyl) benzene sulfonamide (AEBS) was anchored onto nanovesicles loaded with hemoglobin (Hb) and chlorin e6 (Ce6). Upon reaching tumor regions, PAHC could be internalized by cancer cells specifically by means of CA IX targeting and intervention. Afterwards, the binding of AEBS could elicit intracellular acidification and alter redox homeostasis to boost the lipid peroxidation (LPO) level, thus aggravating the ferroptosis process. Meanwhile, Hb served as an iron reservoir that could efficiently evoke ferroptosis and release O_2 to ameliorate tumor hypoxia. With the help of self-supplied O_2, Ce6 produced a plethora of $^1O_2$ for enhanced photodynamic therapy, which in turn favored LPO accumulation to synergize ferroptosis. This study presents a promising paradigm for designing nanomedicines to heighten ferroptosis-based synergetic therapeutics through remodeling the intracellular environment.

New concepts

Ferroptosis-based cancer therapy is still severely impeded by the aberrant cellular metabolic status. This work demonstrated a nanovesicle-potentiated ferroptosis by remodeling the tumor intracellular environment. A novel and simple assembly of tumor-associated transmembrane protein (CA IX) inhibitor (AEBS) conjugated with PLGA-PEG, hemoglobin (Hb) and a photosensitizer (Ce6) created a nanovesicle that specifically recognized CA IX receptors on cancer cells. The binding of CA IX inhibitors could elicit intracellular acidification and alter redox homeostasis to boost the lipid peroxidation (LPO) level. The encapsulation of Hb and Ce6 could not only evoke ferroptosis through its metabolism but also ameliorate tumor hypoxia, which in turn enhances LPO accumulation to synergize ferroptosis. This study pioneers a compelling strategy for designing ferroptosis-based nanomedicine through remodeling the tumor intracellular environment.

1. Introduction

The regulated cell death (RCD) process can be differentially activated in specific pathological states and affect tumor progression, thus being recognized as a potential avenue for selective tumor elimination.[1–3] Among them, ferroptosis, an emerging RCD mode that features the intracellular accumulation of iron and lipid peroxidation (LPO), has recently aroused considerable concern for cancer management.[4,5] Mechanistically, the ferroptosis-related oxidation effect has been illuminated by the iron-dependent Fenton reaction, in which iron reacts with H_2O_2 to furnish highly oxidative $^{\bullet}OH$ for inducing intracellular oxidative stress and lesions, exhibiting LPO and subsequent plasma membrane rupture.[6,7] Consequently, the upregulation of intracellular iron content can perturb iron homeostasis and result in ferroptosis.[8] However, such ferroptosis cell death was still severely impeded by the aberrant cellular metabolic status comprising high GSH level (10 mM), highly active glutathione peroxidase 4 (GPX4), intracellular alkaline pH (pHi 7.2–7.5), *etc.*[9–11] Therefore, upsetting cellular antioxidant homeostasis is a prior strategy to promote tumorous ferroptosis for cancer treatment.

Carbonic anhydrase IX (CA IX) is a tumor-associated transmembrane protein for regulating intratumoral pH, which contributes to tumor proliferation.[12,13] Recently, CA IX has been unveiled to affect cellular metabolism and is critical to maintaining redox homeostasis.[9] Suppression of CA IX activity could significantly mediate intracellular acidification and trigger

[a] *Fujian Provincial Key Laboratory of Innovative Drug Target Research, School of Pharmaceutical Sciences, Xiamen University, Xiamen 361102, China. E-mail: liangxj@nanoctr.cn, zhuxuan@xmu.edu.cn, huosd@xmu.edu.cn*

[b] *School of Medicine, Xiamen University, Xiamen 361102, China*

[c] *Xiamen Key Laboratory of Respiratory Diseases, Department of Basic Medicine, Xiamen Medical College, Xiamen 361023, China*

[d] *CAS Key Laboratory for Biomedical Effects of Nanomaterials and Nanosafety, CAS Center for Excellence in Nanoscience, National Center for Nanoscience and Technology of China, Beijing 100190, China*

[e] *University of Chinese Academy of Sciences, Beijing 100049, China*

† Electronic supplementary information (ESI) available: Chemicals, synthesis, cell culture, and additional experimental details and figures. See DOI: https://doi.org/10.1039/d2nh00494a

intracellular redox homeostasis more susceptible to ferroptosis. As a tumor-overexpressed membrane receptor, CA IX has garnered much interest as a potential target in tumor-specific therapy.[14–16] Nanomedicines anchored with CA IX inhibitors could realize active tumor-targeting delivery and efficient intratumoral enrichment through the specific ligand–receptor interaction.[17–19] Although CA IX inhibitors can remodel the intracellular environment to potentiate ferroptosis, such strategies have remained largely unexplored.

Recent studies pointed out that, as one kind of reactive oxygen species (ROS), $^1O_2$ contributes to lipid peroxidation in synergism with ferroptosis inducers.[20] Meanwhile, the highly toxic $^1O_2$ produced by photodynamic therapy (PDT) can irreversibly damage the DNA structure.[21–23] Thus, the combination of PDT with ferroptosis could harness the striking potential of synergetic cancer therapy. Furthermore, benefiting the ferroptosis-inducing and O_2 donor abilities, the introduction of hemoglobin (Hb) could attenuate tumor hypoxia and boost the therapeutic effect to a greater extent.[24–27]

Herein, we developed a CA IX-targeted nanovesicle called PAHC NV, which could acidify intracellular pH and perturb cellular redox homeostasis to induce and potentiate ferroptosis (Scheme 1). The nanovesicle was assembled by CA IX inhibitor 4-(2-aminoethyl) benzene sulfonamide (AEBS), conjugated with poly(lactide-coglycolide)-poly(ethylene glycol)-NHS (PLGA-PEG-NHS), photosensitizer chlorin e6 (Ce6) and Hb. Upon reaching tumor regions, the PAHC NV could specifically recognize and bind with CA IX receptors on cancer cells and subsequently be internalized into the cytoplasm. Meanwhile, the AEBS blocking suppressed the CA IX activity to facilitate intracellular acidosis and induce susceptibility in redox homeostasis, thus boosting LPO accumulation and potentiating ferroptosis. The results proved that the encapsulation of Hb could not only evoke ferroptosis through its metabolism, but also ameliorate tumor hypoxia with released O_2 thus enhancing the Ce6-triggered PDT. Additionally, the produced $^1O_2$ further enhances the therapeutic effect by contributing to lipid peroxidation in synergism with ferroptosis cell death. Besides, the fluorescence (FL) imaging
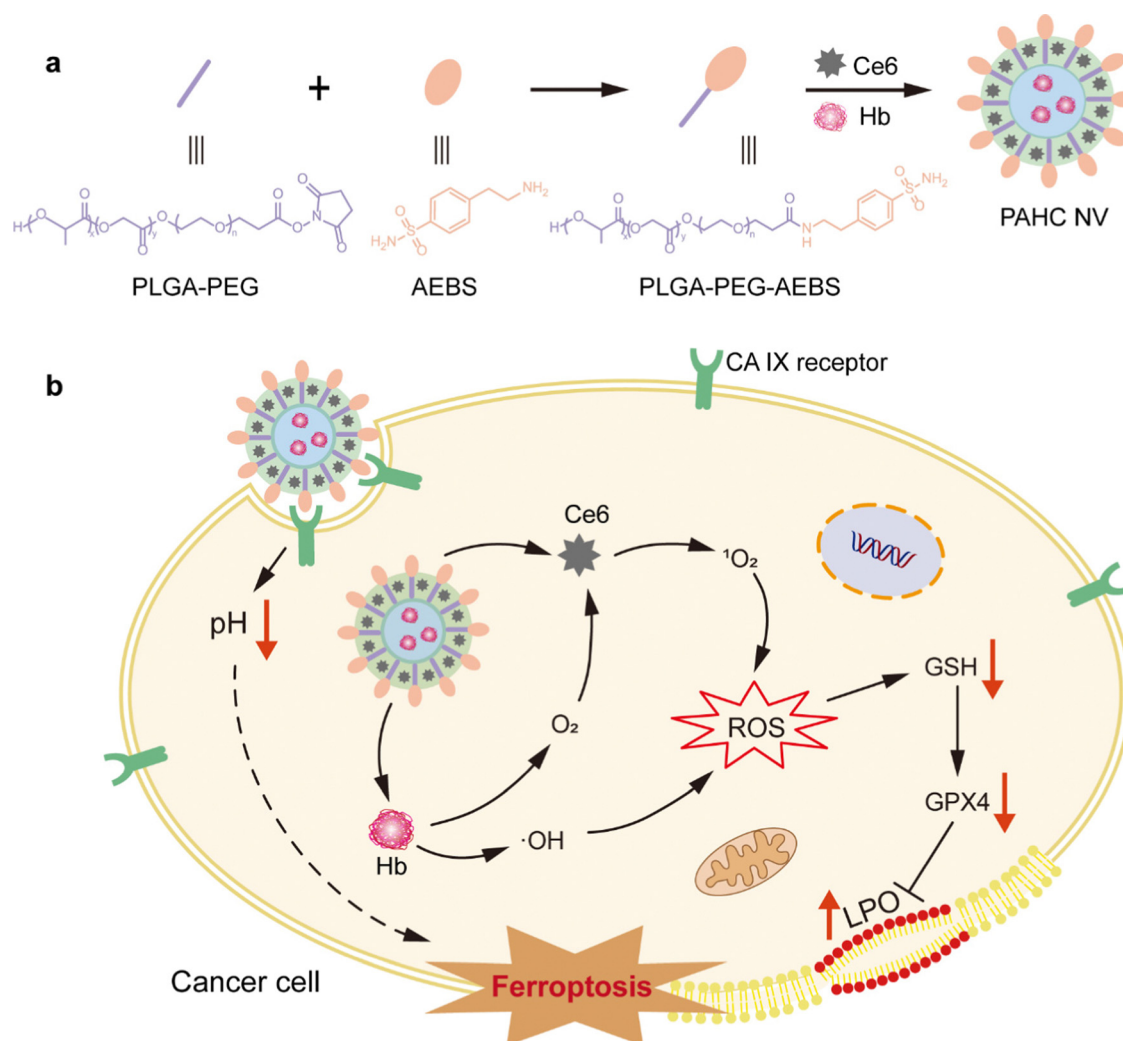
Scheme 1 Schematic diagram of CA IX-targeted PAHC NV potentiated ferroptosis by remodeling the intracellular environment for synergetic cancer therapy. (a) Illustration of the preparation of the PAHC NV. (b) The proposed mechanism of the PAHC NV potentiated tumor ferroptosis.

results demonstrated the efficient delivery and accumulation of the PAHC NV at the tumor site. Overall, the fabrication of the CA IX-targeted PAHC NV provides a promising paradigm to potentiate ferroptosis-based therapeutics and synergetic cancer therapy.

2. Results and discussion

2.1. Preparation and characterization of the PAHC NV

CA IX-targeted PLGA-PEG-AEBS was synthesized by the conjugation of amphiphilic copolymer PLGA-PEG-NHS and CA IX inhibitor AEBS *via* an amidation reaction (Fig. S1, ESI†). [1]H nuclear magnetic resonance spectroscopy (Fig. 1a) and Fourier transform infrared spectroscopy (Fig. 1b) were conducted to validate the structures of PLGA-PEG-AEBS. The typical UV-vis absorption peak of AEBS at 225 nm was detected in the absorption spectrum of PLGA-PEG-AEBS, which further authenticates the successful synthesis of the CA IX-targeted polymer (Fig. 1c) and the number-average molecular weight of PLGA-PEG-AEBS was about 5 kDa (Fig. S2, ESI†).[28] Next, the PAHC NV was constructed *via* a one-step self-assembly process in an aqueous solution through multiple weak interactions containing π–π stacking and electrostatic interactions.[29–31]

The morphology and particle size of the PAHC NV were separately revealed by transmission electron microscopy (TEM) and dynamic light scattering (DLS), exhibiting uniform spheres and a hydrodynamic particle size of 144.6 nm (Fig. 1d and e). The slight difference between the TEM and DLS results could be attributed to the different hydration states during the measurement process.[32] Of note, the ζ-potential of the PAHC NV was negative (-16.2 ± 0.5 mV), meaning that the PAHC NV could remain stable in the bloodstream for the electrostatic repulsion effect (Fig. S3, ESI†). Then the UV-vis absorption (Fig. 1f) and FL spectrum (Fig. 1g) were conducted to testify that Ce6 was successfully encapsulated into the nanovesicle. Besides, the SDS-PAGE-based protein analysis results and energy dispersive spectroscopy (EDS) demonstrate that Hb was also decorated in such nanovesicles (Fig. 1h and Fig. S4, ESI†). Meanwhile, the loading efficiencies of Ce6 and Hb were determined to be 3.9% and 9.4%, respectively. To explore the physiological stability of the obtained nanovesicles, DLS was implemented to monitor the particle size and PDI variation at preset time points. As shown in Fig. 1i, the hydrodynamic diameter and dispersity of the PAHC NV disclosed no remarkable alterations. The results illustrated that the PAHC NV
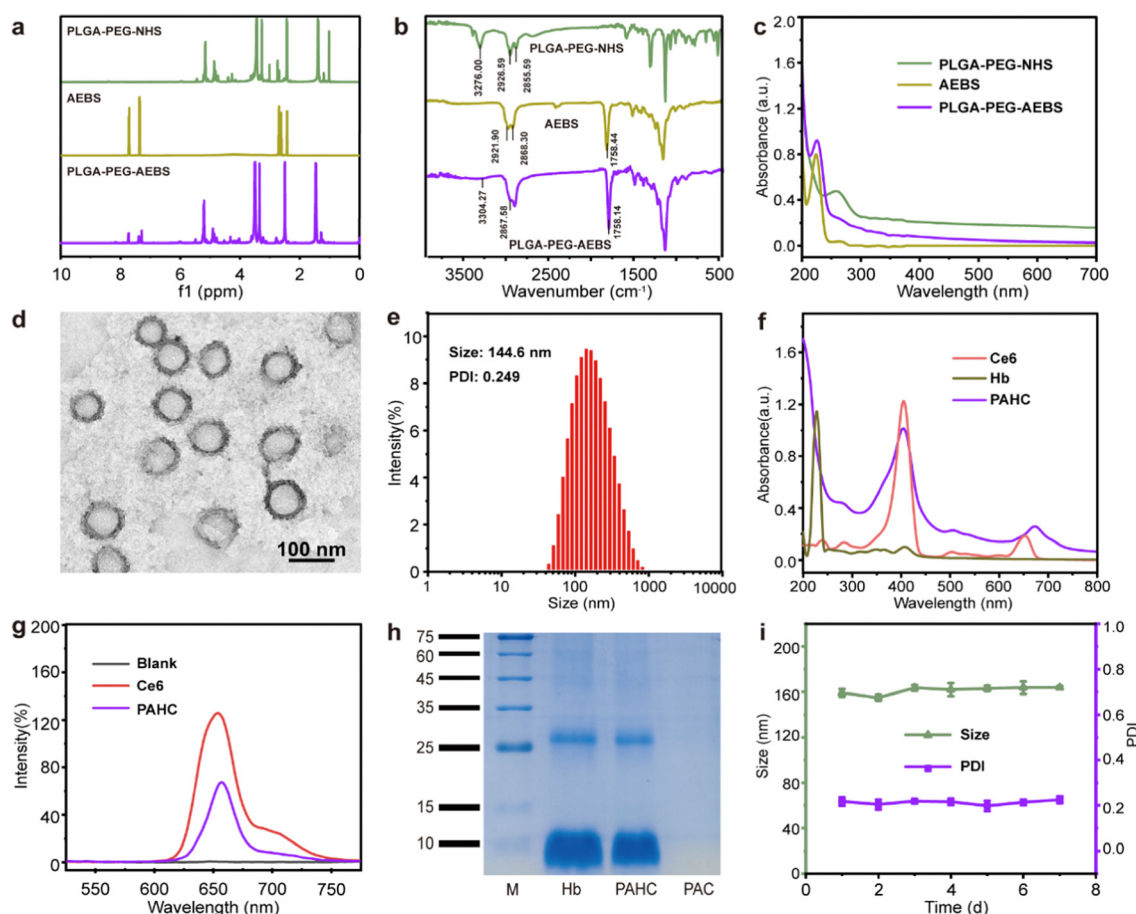
Fig. 1 Preparation and characterization of the PAHC NV. (a) ^{1}H NMR spectrum, (b) FT–IR spectra, and (c) UV-vis absorption spectra of compound PLGA-PEG-NHS, AEBS, and PLGA-PEG-AEBS, respectively. (d) TEM image and (e) particle size distributions of the PAHC NV. (f) UV-vis absorption spectra of Ce6, Hb, and the PAHC NV. (g) Fluorescence spectra of Ce6 and the PAHC NV. (h) SDS-PAGE protein tracking of Hb, PAC, and the PAHC NV. (i) Hydrodynamic diameter and PDI changes of the PAHC NV.

possesses superb structural stability and great potential for further *in vitro* and *in vivo* studies.

2.2. ROS production ability and oxygen release behavior of the PAHC NV

ROS, such as $^{\bullet}OH$ and $^1O_2$, play critical roles in eliminating cancer cells by damaging the structure of proteins and DNA to induce apoptosis, or lipid peroxidation accumulation resulting in ferroptosis. We first inspected the $^{\bullet}OH$ generation of PAHC nanovesicles using 3,3′,5,5′-tetramethylbenzidine (TMB) as a ROS capture probe, in which a plethora of iron within Hb could catalyze H_2O_2 to initiate the Fenton reaction and lead to the absorbance variation. As shown in Fig. 2a, the typical absorbance peak at 651 nm gradually increased as the reaction time prolonged, suggesting the efficient ROS-producing ability of the PAHC NV. To further explore the $^{\bullet}OH$ generation property of the PAHC NV, electron spin resonance (ESR) spectrometry was applied. As illustrated in Fig. 2b, in contrast with the control group (H_2O), a prominent $^{\bullet}OH$ signal (1:2:2:1) was observed when Hb solution was co-incubated with 5,5-dimethyl-1-pyrroline-*N*-oxide (DMPO).[33] Similar to the Hb group, the PAHC

NV could also produce $^{\bullet}OH$ radicals, meaning that the Hb-mediated Fenton activity was still conserved after being encapsulated into nanovesicles. In addition to upregulating the ROS levels, Hb could also be used as an oxygen supplier. Therefore, the oxygen release behavior of Hb was inspected with a tris(4,7-diphenyl-1,10-phenanthroline)ruthenium (II) dichloride ($Ru(dpp)_3Cl_2$) probe.[34] As shown in Fig. 2c and d, the fluorescence intensity at 610 nm displayed no apparent variation with the prolonging of the time in the control group (deoxygenated water), whereas a sharp fluorescence quenching phenomenon was observed for the Hb and PAH group, which testified that the PAH still preserved the oxygen-carrying capabilities. It is worth noting that the difference between PAH and Hb could be attributed to the retarding effect of nanovesicles on the oxygen-releasing ability.

Considering that the PDT efficiency is closely relevant to the local oxygen content, we next explored the $^1O_2$ generation of such O_2 self-supply nanovesicles with the ESR spectrum.[35] As depicted in Fig. 2e, the intensity of the typical 1:1:1-signal peak matching $^1O_2$ species in the Ce6 group disclosed no noticeable difference in contrast with the deoxygenated H_2O group. Obviously, a marked enhancement of $^1O_2$ in the PAHC NV group could be detected,

Fig. 2 ROS production ability and oxygen release behavior study of the PAHC NV. (a) The UV-vis absorption profiles of TMB after being treated with PAHC for different time periods. (b) ESR spectra of the $^{\bullet}OH$ generation after coincubation with Hb and PAHC. (c) The fluorescence spectral changes of $Ru(dpp)_3Cl_2$ after coincubation with deoxygenated water, Hb, and PAH. (d) The O_2 release ability of Hb and PAH; I_0 and I_n represent the fluorescence intensity of the O_2 probe at different time points. (e) ESR spectra of the $^1O_2$ generation after coincubation with Ce6 and PAHC in hypoxia. (f) The fluorescence spectrum of ABDA after coincubation with deoxygenated water, Ce6, and PAHC in hypoxia. (g) The decay rate of ABDA fluorescence curves after coincubation with Ce6 and PAHC in hypoxia.

indicating that the combination of Hb and Ce6 could improve the $^1O_2$ production due to the O_2 self-supply ability. Besides, we further quantitatively evaluated the $^1O_2$ production efficiency with 9,10-anthracenediyl-bis(methylene)-dimalonic acid (ABDA) as a fluorescence probe (Fig. 2f–g).[36] In contrast with Ce6, the PAHC NV resulted in an obvious fluorescence decay, and the FL intensity diminished from 69% to 26%. Therefore, we supposed that the PAHC NV could efficiently achieve PDT in hypoxia due to the presence of Hb for oxygen self-supply.

2.3. Selective cellular uptake, pH regulation, and intracellular ROS production of the PAHC NV

To evaluate the nanovesicles' selective cellular uptake capacity, 4T1 cells with overexpressed CA IX receptors were treated with different formulations.[37] Confocal laser scanning microscopy (CLSM) and flow cytometry were implemented to acquire the qualitative and quantitative cellular uptake assessments. As exhibited in Fig. 3a, 4T1 cells treated with PHC (without AEBS functionalization) manifested slightly weak red fluorescence of Ce6 within the cytoplasm, while a bright red fluorescence could be detected in PAHC-treated cells, indicating that AEBS modification dramatically improved the internalization efficiency of PAHC NVs via CA IX receptor-mediated endocytosis. To further illustrate the specific cellular uptake effect of the PAHC NV, 4T1 cells were pretreated with AEBS before incubating with PAHC NVs. As expected, the red fluorescence intensity was as weak as that in the PHC group, manifesting that AEBS was competitively bound with CA IX receptors on the cell membrane, blocking the recognition and endocytosis of the PAHC NVs. The results obtained from flow cytometry were consistent with that in CLSM images (Fig. 3b), demonstrating that PAHC NVs could be effectively phagocytized by 4T1 cells through the CA IX receptor-mediated endocytosis pathway.

Next, the excellent cellular uptake capacity of the PAHC NV inspired us to evaluate its intracellular pH regulation capability. We utilized 2′,7′-bis(2-carboxyethyl)-5(6)-carboxyfluorescein acetoxymet (BCECF-AM), a pH-sensitive probe, to monitor the intracellular pH changes of 4T1 cells after being treated with different formulations.[38] As shown in Fig. 3c, a bright green fluorescence signal was observed in the control group (PBS-treated) due to the high pH value in the cytoplasm. Compared with the control group, the fluorescence intensity of Hb, Ce6, and PHC treated cells displayed little changes, while the signal attenuated significantly in the groups treated with PAHC and PAHC (AEBS pretreated). Furthermore, the pH change was measured using the BCECF-AM probe, and compared with the control groups (pH = 7.4, 7.2. 7.0, 6.8, 6.6), the intracellular pH of PAHC-treated cells significantly dropped from pH 7.4 to ∼6.6 (Fig. S5, ESI†). The results illustrated that AEBS modifications conferred the PAHC NV with the inhibition effect of CA IX and induced intracellular acidification.

Since acidosis could trigger intracellular redox homeostasis more susceptible to promoting cellular ROS accumulation for potentiating ferroptosis,[9] we next estimated the cellular ROS level of 4T1 cells by employing a ROS indicator (dichlorofluorescein diacetate, DCFH-DA). As shown in Fig. 3d, in contrast

with the PBS group, Hb-treated cells exhibited slightly weak green fluorescence both in normoxic and hypoxic environments, which can be accredited to the fact that Hb-mediated Fenton reaction elevated the intracellular $^{\bullet}OH$ levels. The fluorescence intensity of Ce6-treated cells in normoxia was brighter than that in hypoxia because PDT was O_2-dependent and hypoxia seriously compromised the $^1O_2$ generation efficiency. Due to the enhanced internalization efficiency and acidified intracellular pH, a stronger fluorescence was detected in the PAHC NV group, manifesting the production of massive ROS within PAHC-treated cells.

As excessive intracellular ROS could affect the normal functions of mitochondria, the mitochondrial membrane potential variation was monitored with the JC-1 fluorescent probe after being cultured with different formulations.[39] As shown in Fig. 3e, the brightest red fluorescence was observed in the PBS group, implying relatively healthy mitochondria. After being treated with Ce6 or PHC, amplified green fluorescence and decreased red fluorescence were detected, suggesting that the mitochondrial membrane potential was lost in these groups. By comparison, 4T1 cells treated with PAHC NVs represented the brightest green fluorescence, indicating that PAHC NVs caused severe damage to mitochondrial functions. Collectively, the constructed PAHC NV could serve as a promising nanovesicle in causing intracellular ROS accumulation and mitochondrial dysfunction for ferroptosis cell death.

2.4. In vitro cytotoxicity evaluation of the PAHC NV

Given that ROS level elevation and mitochondrial damage usually result in ferroptosis and apoptosis, we next introduced the MTT assay to examine the cytotoxicity of the PAHC NV. 4T1 cells were incubated with different formulations, and the cytotoxic effects under normoxia and hypoxia were compared. As shown in Fig. 4a and b, significant cytotoxicity was observed in the PAHC NV treated group and its cytotoxic effect displayed no apparent difference between normoxic and hypoxic conditions. The cytotoxicity results were further confirmed with the calcein-acetoxymethyl ester/propidium iodide (PI) staining assay. As shown in Fig. 4c, the PAHC NV treated cells displayed the brightest red fluorescence, demonstrating the efficient cancer cell-killing capacity of the PAHC NV. In addition, the Annexin V-FITC/PI-mediated apoptosis co-staining assay was applied to quantify the therapeutic efficiency of the PAHC NV further. As depicted in Fig. S6 and S7 (ESI†), the apoptosis rate of Ce6-treated cells in hypoxic conditions was 8.4%, while it increased to 20.7% in normoxic conditions. The most severe apoptosis was detected in the PAHC NV groups, which might be accredited to the CA IX receptor-mediated internalization and intracellular microenvironment remodeling of cancer cells.

We next proved that the PAHC NV induced intracellular LPO accumulation by staining 4T1 cells with C11-BODIPY$^{581/591}$ as an intracellular LPO probe. As shown in Fig. 4d, in contrast with the PHC-treated group, a significant decayed red fluorescence and intensified green fluorescence was observed in the PAHC group, suggesting that the AEBS modification of NV accelerates the intracellular LPO accumulation. Notably, the addition of Lip-1, a ferroptosis inhibitor, could evidently reverse the PAHC-induced LPO increase and ferroptosis cell death.

Fig. 3 Selective cellular uptake, pH regulation, and intracellular ROS production of the PAHC NV. The cellular uptake behavior of Ce6, PHC, and PAHC was studied by (a) CLSM images and (b) flow cytometric analysis after incubation for 6 h. For the PAHC (AEBS pretreated) group, 4T1 cells were pretreated with AEBS for 2 h. (c) BCECF-stained (a pH-sensitive probe), and (d) DCFH-stained (a ROS indicator) 4T1 cells after coincubation with PBS, Hb, Ce6, PHC, PAHC and PAHC (AEBS pretreated), respectively. (e) CLSM images of mitochondrial membrane potential detection in 4T1 cells after coincubation with PBS, Hb, Ce6, PHC, PAHC and PAHC (AEBS pretreated), respectively.

Besides, a malondialdehyde (MDA) kit was also implemented to quantify cellular LPO levels.[40] As shown in Fig. 4e, the MDA amounts in PAHC NV treated cells significantly increased compared with the PBS group, manifesting that the PAHC NV effectively triggered the LPO accumulation and ferroptosis response of cancer cells. Since the glutathione peroxidase 4 (GPX4)-glutathione (GSH) system is one of the major ferroptosis defense systems for LPO elimination.[41] The GPX4 expression and GSH amounts were also measured for *in vitro* ferroptosis analysis. As displayed in Fig. 4f–h, compared with the PHC-treated groups, the PAHC NV significantly down-regulated the GPX4 expression, GPX4 activity, and intracellular GSH levels. These results further illustrated that AEBS-anchored nanovesicles could potentiate ferroptosis through interaction with CA IX receptors.
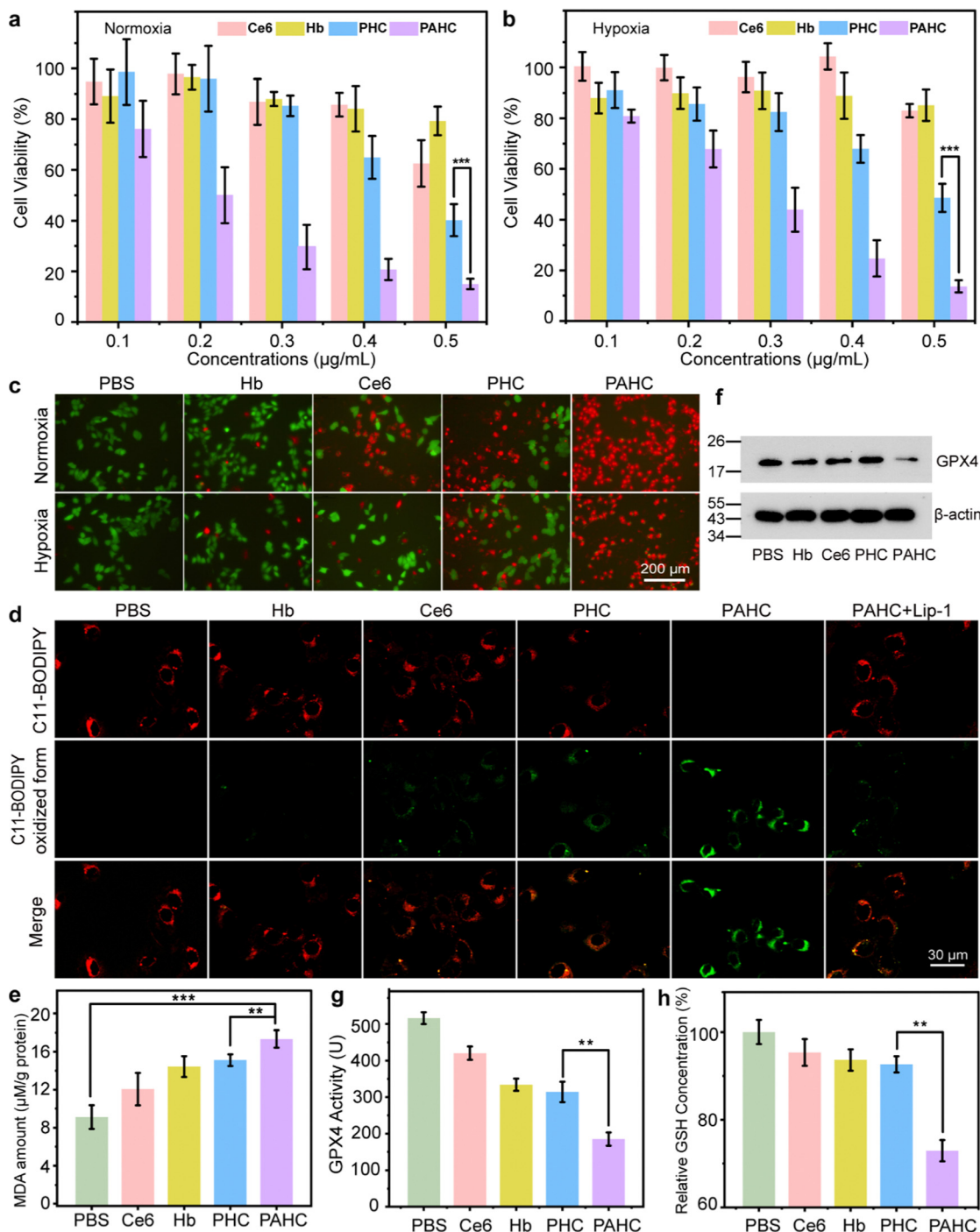
Fig. 4 *In vitro* cytotoxicity evaluation of PAHC NV. Cell viability of 4T1 cells after being treated with PBS, Ce6, Hb, PHC, and PAHC under (a) normoxia and (b) hypoxia. (c) Calcein-AM (live cells, green fluorescence) and PI (dead cells, red fluorescence) staining images of 4T1 cells and (d) cellular LPO accumulations of 4T1 cells after treatment with Hb, Ce6, PHC, PAHC and PAHC + Lip-1 and subsequently stained C11-BODIPY$^{581/591}$ dye. (e) Cellular LPO levels probed by MDA amount of 4T1 cells incubated with PBS, Ce6, Hb, PHC, and PAHC. (f) Western blot analysis of GPX4 expression in 4T1 cells after incubation with Hb, Ce6, PHC, and PAHC. (g) GPX4 activity and (h) GSH level of 4T1 cells incubated with PBS, Ce6, Hb, PHC, and PAHC, respectively.

2.5. *In vivo* biodistribution and ferroptosis-based antitumor efficacy assessment of PAHC NV

Encouraged by the excellent therapeutic efficacy of the PAHC NV at the cellular level, we next monitored its biodistribution and ferroptosis-based antitumor efficacy using the 4T1 tumor-bearing mouse model (Fig. 5a).[42] As shown in Fig. 5b, without AEBS modification, the FL intensity in the PHC group was faint at the tumor region while intense at the liver site. In contrast, considerable FL signals were observed at the tumor site in the PAHC NV group, indicating the tumor targeting and enrichment behavior of
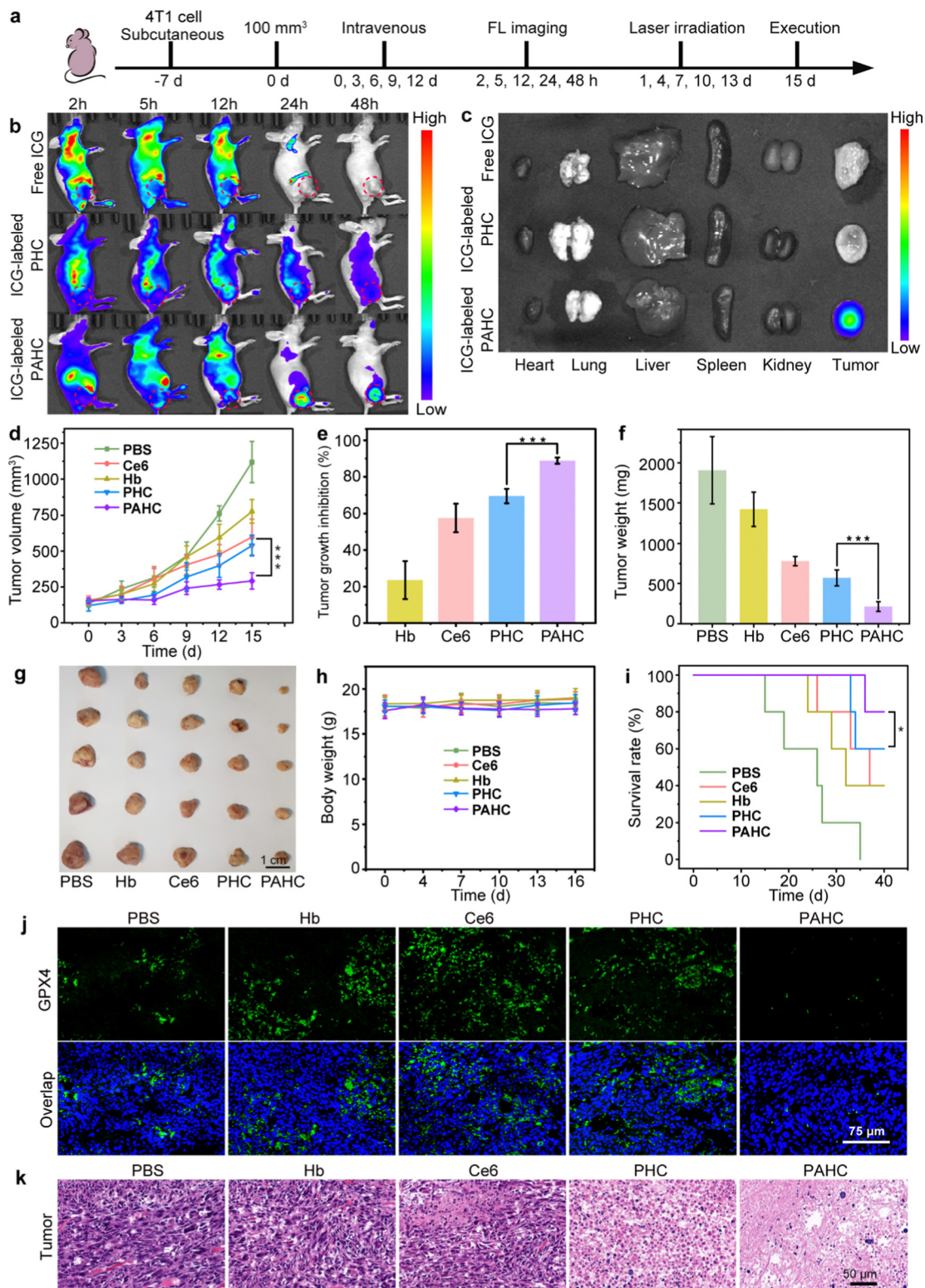
Fig. 5 *In vivo* biodistribution and ferroptosis-based antitumor efficacy assessment of the PAHC NV. (a) Diagrammatic representation of the timeline for therapeutic treatment and FL imaging *in vivo*. (b) The *in vivo* biodistribution at 2, 5, 12, 24, and 48 h post-injection. The tumor site was circled. (c) Fluorescence imaging of excised main organs and tumors at 48 h post-injection. (d) Tumor growth curves during the therapeutic period (*n* = 5). (e) Tumor inhibition rate, (f) weights, and (g) images of the dissected tumors after being treated with PBS, Ce6, Hb, PHC, and PAHC. (h) Body weight variations and (i) survival curve of the mice. (j) GPX4 immunohistochemical analysis of tumor tissues after treatment with Hb, Ce6, PHC, and PAHC (green color indicates the GPX4 level). (k) H&E-stained tumor sections at 15 days.

the PAHC NV. The quantitative analysis indicates that the amount of PAHC NV within the tumor regions was *Ca.* 2.48-fold than that of PHC at 24 h (Fig. S8a, ESI†). In addition, the result of *ex vivo* fluorescence imaging and intensity analysis of the excised major organs and tumor tissues verified that the PAHC NV achieved prominent tumor-specific accumulation in the presence of AEBS modification (Fig. 5c and Fig. S8b, ESI†).

Next, the *in vivo* ferroptosis-based therapeutic benefits were explored with 4T1 tumor-bearing mice. As illustrated in Fig. 5d–g and Fig. S9 (ESI†), comparing the average tumor volumes of other groups, the PAHC NV treated mice achieved an overwhelming tumor inhibition efficiency (88%), suggesting that AEBS-mediated CA IX targeting and tumor intracellular environment remodeling significantly increased the ferroptosis-based therapeutic effect. The PAHC NV treatment led to a pronouncedly prolonged survival period of tumor-bearing mice without any body weight loss (Fig. 5h–i). All the mice in the PAHC-treated group were kept alive on the 36th day, while all untreated tumor-bearing mice of the control group were sacrificed. The *in vivo* GPX4 deactivation performance of PAHC-treated ferroptosis was further estimated by an immunohistological study. As displayed in Fig. 5j, negligible green fluorescence could be observed in the PAHC group as compared with the PHC treated group, indicating that CA IX inhibitor could significantly down-regulate intra-tumoral GPX4 for potentiating ferroptosis cell death. Besides, a hematoxylin–eosin (H&E) staining assay was implemented to further testify the antitumor effect of the PAHC NV. As shown in Fig. 5k, the PAHC NV caused the most severe tumor cell damage among all formulations, revealing that the PAHC NV could efficiently suppress tumor development by targeting CA IX and potentiated ferroptosis. Meanwhile, the biosafety of the PAHC NV was tested by hemolytic assay, H&E staining assay, and serum biochemical index analysis (Fig. S10–S12, ESI†), demonstrating that the nanovesicle is capable of outstanding biocompatibility properties and no apparent systemic toxicity during *in vivo* applications.[43,44]

3. Conclusion

In summary, we have constructed a CA IX-targeted nanovesicle for potentiating ferroptosis through remodeling the intracellular environment. The AEBS modification enables nanovesicles with excellent tumor targeting and enrichment. More importantly, the selective binding of AEBS with the CA IX receptor could acidify the intracellular pH and perturb redox homeostasis to enhance the ferroptosis-based synergistic therapy. Taken together, our study pioneers an effective and compelling avenue in designing ferroptosis-based nanomedicine for enhanced cancer therapy through intracellular environment remodeling.

Conflicts of interest

The authors declare no competing financial interest.

Acknowledgements

References

1 S. J. Dixon, K. M. Lemberg, M. R. Lamprecht, R. Skouta, E. M. Zaitsev, C. E. Gleason, D. N. Patel, A. J. Bauer, A. M. Cantley, W. S. Yang, B. Morrison, 3rd and B. R. Stockwell, Ferroptosis: an iron-dependent form of nonapoptotic cell death, *Cell*, 2012, **149**(5), 1060–1072.

2 L. Van der Meeren, J. Verduijn, D. V. Krysko, A. G. Skirtach and A. F. M. Analysis, Enables Differentiation between Apoptosis, Necroptosis, and Ferroptosis in Murine Cancer Cells, *iScience*, 2020, **23**(12), 101816.

3 S. Huo, M. Kwak, J. Qin, B. Dittrichn and A. Herrmann, Dynamic DNA-based biomaterials interacting with external, macroscopic, and molecular stimuli, *Mater. Today*, 2021, **49**, 378–390.

4 X. Chen, R. Kang, G. Kroemer and D. Tang, Broadening horizons: the role of ferroptosis in cancer, *Nat. Rev. Clin. Oncol.*, 2021, **18**(5), 280–296.

5 G. Tang, J. He, J. Liu, X. Yan and K. Fan, Nanozyme for tumor therapy: Surface modification matters, *Exploration*, 2021, **1**(1), 75–89.

6 X. Jiang, B. R. Stockwell and M. Conrad, Ferroptosis: mechanisms, biology and role in disease, *Nat. Rev. Mol. Cell Biol.*, 2021, **22**(4), 266–282.

7 H. F. Yan, T. Zou, Q. Z. Tuo, S. Xu, H. Li, A. A. Belaidi and P. Lei, Ferroptosis: mechanisms and links with diseases, *Signal Transduction Targeted Ther.*, 2021, **6**(1), 49.

8 H. Liang, X. Wu, G. Zhao, K. Feng, K. Ni and X. Sun, Renal Clearable Ultrasmall Single-Crystal Fe Nanoparticles for Highly Selective and Effective Ferroptosis Therapy and Immunotherapy, *J. Am. Chem. Soc.*, 2021, **143**(38), 15812–15823.

9 S. C. Chafe, F. S. Vizeacoumar, G. Venkateswaran, O. Nemirovsky, S. Awrey, W. S. Brown, P. C. McDonald, F. Carta, A. Metcalfe, J. M. Karasinska, L. Huang, S. K. Muthuswamy, D. F. Schaeffer, D. J. Renouf, C. T. Supuran, F. J. Vizeacoumar and S. Dedhar, Genome-wide synthetic lethal screen unveils novel CAIX-NFS1/xCT axis as a targetable vulnerability in hypoxic solid tumors, *Sci. Adv.*, 2021, **7**(35), eabj0364.

10 R. Yue, C. Zhang, L. Xu, Y. Wang, G. Guan, L. Lei, X. Zhang and G. Song, Dual key co-activated nanoplatform for switchable MRI monitoring accurate ferroptosis-based synergistic therapy, *Chem*, 2022, **8**(7), 1956–1981.

11 C. Mao, X. Liu, Y. Zhang, G. Lei, Y. Yan, H. Lee, P. Koppula, S. Wu, L. Zhuang, B. Fang, M. V. Poyurovsky, K. Olszewski and B. Gan, DHODH-mediated ferroptosis defence is a targetable vulnerability in cancer, *Nature*, 2021, **593**(7860), 586–590.

12 D. Neri and C. T. Supuran, Interfering with pH regulation in tumours as a therapeutic strategy, *Nat. Rev. Drug Discovery*, 2011, **10**(10), 767–777.

13 Y. Lou, P. C. McDonald, A. Oloumi, S. Chia, C. Ostlund, A. Ahmadi, A. Kyle, U. Auf dem Keller, S. Leung, D. Huntsman, B. Clarke, B. W. Sutherland, D. Waterhouse, M. Bally, C. Roskelley, C. M. Overall, A. Minchinton, F. Pacchiano, F. Carta, A. Scozzafava, N. Touisni, J. Y. Winum, C. T. Supuran and S. Dedhar, Targeting tumor hypoxia: suppression of breast tumor growth and metastasis by novel carbonic anhydrase IX inhibitors, *Cancer Res.*, 2011, **71**(9), 3364–3376.

14 A. Janoniene, Z. Liu, L. Baranauskiene, E. Makila, M. Ma, J. Salonen, J. Hirvonen, H. Zhang, V. Petrikaite and H. A. Santos, A Versatile Carbonic Anhydrase IX Targeting Ligand-Functionalized Porous Silicon Nanoplatform for Dual Hypoxia Cancer Therapy and Imaging, *ACS Appl. Mater. Interfaces*, 2017, **9**(16), 13976–13987.

15 G. L. Fan, P. Yuan, F. A. Deng, L. S. Liu, Y. L. Miao, C. Wang, X. Z. Qiu, X. Y. Yu, H. Cheng and S. Y. Li, Self-Delivery Photodynamic Nanoinhibitors for Tumor Targeted Therapy and Metastasis Inhibition, *ACS Appl. Bio Mater.*, 2020, **3**(9), 6124–6130.

16 A. Thiry, J. M. Dogne, B. Masereel and C. T. Supuran, Targeting tumor-associated carbonic anhydrase IX in cancer therapy, *Trends Pharmacol. Sci.*, 2006, **27**(11), 566–573.

17 N. Liu, W. Zuo, L. Wu, L. Chen, Z. Xiao, Q. Jin, J. Liu, L. Tu, S. Huo and X. Zhu, Myeloperoxidase-targeted nanotheranostics for self-enhanced synergetic photo/chemo/chemodynamic therapy, *Mater. Today Chem.*, 2022, **23**, 100740.

18 S. Huo, P. Zhao, Z. Shi, M. Zou, X. Yang, E. Warszawik, M. Loznik, R. Gostl and A. Herrmann, Mechanochemical bond scission for the activation of drugs, *Nat. Chem.*, 2021, **13**(2), 131–139.

19 S. Li, W. Su, H. Wu, T. Yuan, C. Yuan, J. Liu, G. Deng, X. Gao, Z. Chen, Y. Bao, F. Yuan, S. Zhou, H. Tan, Y. Li, X. Li, L. Fan, J. Zhu, A. T. Chen, F. Liu, Y. Zhou, M. Li, X. Zhai and J. Zhou, Targeted tumour theranostics in mice via carbon quantum dots structurally mimicking large amino acids, *Nat. Biomed. Eng.*, 2020, **4**(7), 704–716.

20 P. Zhang, C. Liu, W. Wu, Y. Mao, Y. Qin, J. Hu, J. Hu, J. Fu, D. Hua and J. Yin, Triapine/Ce6-loaded and lactose-decorated nanomicelles provide an effective chemo-photodynamic therapy for hepatocellular carcinoma through a reactive oxygen species-boosting and ferroptosis-inducing mechanism, *Chem. Eng. J.*, 2021, **425**, 131543.

21 J. Chen, X. Tan, Y. Huang, C. Xu, Z. Zeng, T. Shan, Z. Guan, X. Xu, Z. Huang and C. Zhao, Reactive oxygen species-activated self-amplifying prodrug nanoagent for tumor-specific Cu-chelate chemotherapy and cascaded photodynamic therapy, *Biomaterials*, 2022, **284**, 121513.

22 U. Bazylinska, D. Wawrzynczyk, J. Kulbacka, G. Picci, L. S. Manni, S. Handschin, M. Fornasier, C. Caltagirone, R. Mezzenga and S. Murgia, Hybrid Theranostic Cubosomes for Efficient NIR-Induced Photodynamic Therapy, *ACS Nano*, 2022, **16**(4), 5427–5438.

23 L. Tu, Z. Liao, Z. Luo, Y. L. Wu, A. Herrmann and S. Huo, Ultrasound-controlled drug release and drug activation for cancer therapy, *Exploration*, 2021, **1**(3), 20210023.

24 Y. Wang, S. Luo, Y. Wu, P. Tang, J. Liu, Z. Liu, S. Shen, H. Ren and D. Wu, Highly Penetrable and On-Demand Oxygen Release with Tumor Activity Composite Nanosystem for Photothermal/Photodynamic Synergetic Therapy, *ACS Nano*, 2020, **14**(12), 17046–17062.

25 L. Erlandsson, Z. Masoumi, L. R. Hansson and S. R. Hansson, The roles of free iron, heme, haemoglobin, and the scavenger proteins haemopexin and alpha-1-microglobulin in preeclampsia and fetal growth restriction, *J. Intern. Med.*, 2021, **290**(5), 952–968.

26 B. Hassannia, P. Vandenabeele and T. Vanden Berghe, Targeting Ferroptosis to Iron Out Cancer, *Cancer Cell*, 2019, **35**(6), 830–849.

27 Q. Li, X. Han, X. Lan, Y. Gao, J. Wan, F. Durham, T. Cheng, J. Yang, Z. Wang, C. Jiang, M. Ying, R. C. Koehler, B. R. Stockwell and J. Wang, Inhibition of neuronal ferroptosis protects hemorrhagic brain, *JCI Insight*, 2017, **2**(7), e90777.

28 W. Zuo, W. Chen, J. Liu, S. Huang, L. Chen, Q. Liu, N. Liu, Q. Jin, Y. Li, P. Wang and X. Zhu, Macrophage-Mimic Hollow Mesoporous Fe-Based Nanocatalysts for Self-Amplified Chemodynamic Therapy and Metastasis Inhibition via Tumor Microenvironment Remodeling, *ACS Appl. Mater. Interfaces*, 2022, **14**(4), 5053–5065.

29 U. K. Sukumar, J. C. B. Rajendran, S. S. Gambhir, T. F. Massoud and R. Paulmurugan, SP94-Targeted Triblock Copolymer Nanoparticle Delivers Thymidine Kinase-p53-Nitroreductase Triple Therapeutic Gene and Restores Anti-cancer Function against Hepatocellular Carcinoma *In Vivo*, *ACS Appl. Mater. Interfaces*, 2020, **12**(10), 11307–11319.

30 X. Chen, Y. Liu, Y. Wen, Q. Yu, J. Liu, Y. Zhao, J. Liu and G. Ye, A photothermal-triggered nitric oxide nanogenerator combined with siRNA for precise therapy of osteoarthritis by suppressing macrophage inflammation, *Nanoscale*, 2019, **11**(14), 6693–6709.

31 T. Xu, Y. Ma, Q. Yuan, H. Hu, X. Hu, Z. Qian, J. K. Rolle, Y. Gu and S. Li, Enhanced Ferroptosis by Oxygen-Boosted Phototherapy Based on a 2-in-1 Nanoplatform of Ferrous Hemoglobin for Tumor Synergistic Therapy, *ACS Nano*, 2020, **14**(3), 3414–3425.

32 Q. Zhu, Z. Fan, W. Zuo, Y. Chen, Z. Hou and X. Zhu, Self-Distinguishing and Stimulus-Responsive Carrier-Free Theranostic Nanoagents for Imaging-Guided Chemo-Photothermal Therapy in Small-Cell Lung Cancer, *ACS Appl. Mater. Interfaces*, 2020, **12**(46), 51314–51328.

33 C. Wu, Z. Liu, Z. Chen, D. Xu, L. Chen, H. Lin and J. Shi, A nonferrous ferroptosis-like strategy for antioxidant inhibition–synergized nanocatalytic tumor therapeutics, *Sci. Adv.*, 2021, 7(39), eabj8833.

34 Q. Feng, Y. Li, N. Wang, Y. Hao, J. Chang, Z. Wang, X. Zhang, Z. Zhang and L. Wang, A Biomimetic Nanogenerator of Reactive Nitrogen Species Based on Battlefield Transfer Strategy for Enhanced Immunotherapy, *Small*, 2020, **16**(25), e2002138.

35 Y. H. Gao, M. Y. Li, F. Sajjad, J. H. Wang, F. Meharban, M. A. Gadoora, Y. J. Yan, T. Nyokong and Z. L. Chen,

Synthesis and pharmacological evaluation of chlorin derivatives for photodynamic therapy of cholangiocarcinoma, *Eur. J. Med. Chem.*, 2020, **189**, 112049.

36 J. Liu, W. Zuo, Q. Jin, C. Liu, N. Liu, H. Tian and X. Zhu, Mn(II)-directed dual-photosensitizers co-assemblies for multimodal imaging-guided self-enhanced phototherapy, *Mater. Sci. Eng., C*, 2021, **129**, 112351.

37 F. Pacchiano, F. Carta, P. C. McDonald, Y. Lou, D. Vullo, A. Scozzafava, S. Dedhar and C. T. Supuran, Ureido-substituted benzenesulfonamides potently inhibit carbonic anhydrase IX and show antimetastatic activity in a model of breast cancer metastasis, *J. Med. Chem.*, 2011, **54**(6), 1896–1902.

38 Q. He, S. Wu, M. Huang, Y. Wang, K. Zhang, J. Kang, Y. Zhang and F. Quan, Effects of Diluent pH on Enrichment and Performance of Dairy Goat X/Y Sperm, *Front. Cell Dev. Biol.*, 2021, **9**, 747722.

39 H. Yu, J. M. Li, K. Deng, W. Zhou, C. X. Wang, Q. Wang, K. H. Li, H. Y. Zhao and S. W. Huang, Tumor acidity activated triphenylphosphonium-based mitochondrial targeting nanocarriers for overcoming drug resistance of cancer therapy, *Theranostics*, 2019, **9**(23), 7033–7050.

40 H. Zhang, Z. Wang, Z. Liu, K. Du and X. Lu, Protective Effects of Dexazoxane on Rat Ferroptosis in Doxorubicin-Induced Cardiomyopathy Through Regulating HMGB1, *Front. Cardiovasc. Med.*, 2021, **8**, 685434.

41 A. C. Del Valle, C. K. Yeh and Y. F. Huang, Near Infrared-Activatable Platinum-Decorated Gold Nanostars for Synergistic Photothermal/Ferroptotic Therapy in Combating Cancer Drug Resistance, *Adv. Healthcare Mater.*, 2020, **9**(20), e2000864.

42 W. Zuo, N. Liu, Z. Chang, J. Liu, Q. Jin, L. Chen and X. Zhu, Single-site bimetallic nanosheet for imaging guided mutually-reinforced photothermal-chemodynamic therapy, *Chem. Eng. J.*, 2022, **442**, 136125.

43 P. Xue, Q. Li, Y. Li, L. Sun, L. Zhang, Z. Xu and Y. Kang, Surface Modification of Poly(dimethylsiloxane) with Polydopamine and Hyaluronic Acid To Enhance Hemocompatibility for Potential Applications in Medical Implants or Devices, *ACS Appl. Mater. Interfaces*, 2017, **9**(39), 33632–33644.

44 Z. Ren, S. Sun, R. Sun, G. Cui, L. Hong, B. Rao, A. Li, Z. Yu, Q. Kan and Z. Mao, A Metal-Polyphenol-Coordinated Nanomedicine for Synergistic Cascade Cancer Chemotherapy and Chemodynamic Therapy, *Adv. Mater.*, 2020, **32**(6), e1906024.